

RAPID PUBLICATION

Three-dimensional analysis of porous BaTiO₃ ceramics using FIB nanotomography

L. HOLZER, F. INDUTNYI, PH. GASSER, B. MÜNCH & M. WEGMANN

EMPA, Swiss Federal Laboratories for Materials Testing and Research, Ueberlandstrasse 129, 8600 Dübendorf, Switzerland

Key words. Focused ion beam (FIB), microstructure, nanoparticles, particle size distribution, pore size distribution, quantitative analysis, serial sectioning, tomography.

Summary

Three-dimensional (3D) data represent the basis for reliable quantification of complex microstructures. Therefore, the development of high-resolution tomography techniques is of major importance for many materials science disciplines. In this paper, we present a novel serial sectioning procedure for 3D analysis using a dual-beam FIB (focused ion beam). A very narrow and reproducible spacing between the individual imaging planes is achieved by using drift correction algorithms in the automated slicing procedure. The spacing between the planes is nearly of the same magnitude as the pixel resolution on scanning electron microscopy images. Consequently, the acquired stack of images can be transformed directly into a 3D data volume with a voxel resolution of $6 \times 7 \times 17$ nm. To demonstrate the capabilities of FIB nanotomography, a BaTiO₃ ceramic with a high volume fraction of fine porosity was investigated using the method as a basis for computational microstructure analysis and the results compared with conventional physical measurements. Significant differences between the particle size distributions as measured by nanotomography and laser granulometry indicate that the latter analysis is skewed by particle agglomeration/aggregation in the raw powder and by uncertainties related to calculation assumptions. Significant differences are also observed between the results from mercury intrusion porosimetry (MIP) and 3D pore space analysis. There is strong evidence that the ink-bottle effect leads to an overestimation of the frequency of small pores in MIP. FIB nanotomography thus reveals quantitative information of structural features smaller than 100 nm in size which cannot be acquired easily by other methods.

Introduction

With the growing importance of nanotechnology in materials science, the need for high-resolution microscopy is increasing. Various techniques, such as scanning electron microscopy (SEM), transmission electron microscopy (TEM) or atomic force microscopy (AFM), can today reveal details in the nanometre range or even on an atomic scale (e.g. Williams & Carter, 1996; Meyer *et al.*, 2004). However, these methods can only reveal either two-dimensional (2D) or topological information from sections, lamellae or surfaces. Except for the case of highly symmetrical structures, it is impossible to reconstruct 3D geometries from such 2D images. As a consequence, microstructural interpretations based on 2D images usually remain qualitative, or they may be even misleading. A major challenge for many materials science disciplines is thus 3D characterization, which is the basis for parametrization and quantification of microstructural features.

Certain structural characteristics of materials can be determined with physical methods. Particle size distributions of the metal or ceramic powders used to manufacture a bulk component, for example, can be obtained with laser granulometry of the initial nanopowder. However, the effects of subsequent processing steps (e.g. particle packing and thermal sintering) may strongly influence the granular texture in the compacted and densified material. In addition, the results from laser granulometry may be significantly distorted as a result of particle agglomerations in the raw powder. Hence, the final material structure can hardly be deduced from laser granulometry analysis. Similarly, the measurement of pore size distributions by physical methods can be problematical. Mercury intrusion porosimetry (MIP), for instance, is strongly affected by the geometry of pore necks. These invoke the so-called ink-bottle effect, which introduces an important source

of error in MIP measurements (Diamond, 2000). In addition, pore size distributions are not suitable parameters for the characterization of networked structures. Hence, in order to describe granular textures as well as porous networks in detail, it is necessary to establish suitable 3D microscopy methods which can serve as a basis for quantitative microstructural analysis (e.g. Ohser & Mücklich, 2000).

At present, nanoscale resolution in three dimensions can be obtained with transmission microscopy (e.g. electron or X-ray transmission; TEM or TXM, respectively). However, these methods are only applicable to very thin samples (≤ 100 nm in TEM), and this thickness restriction contradicts the requirement of larger volumes that have to be analysed for the reconstruction of continuous network structures. In the following section, the potential uses and limitations of some widely used 3D microscopy methods are briefly discussed. From this review it can be concluded that each of the currently available methods has specific advantages and drawbacks that makes each one suitable only for specific applications. Focused ion beam (FIB) nanotomography, which is presented in this study, enables the 3D reconstruction of microstructural features on the sub-100-nm scale. As such, FIB nanotomography fills the gap between classical tomography methods that operate in the millimetre to micrometre range (e.g. X-ray absorption tomography) and transmission microscopy methods with nanometre resolution (TEM, TXM) but which can only be applied to very thin electron- and photon-transparent samples.

FIB tomography is based on a serial sectioning procedure. In this study we present a methodical refinement of the procedure in which the ultimate goal is to reduce the spacing between the single sections down to less than 20 nm and to reach a similar resolution along all three orthogonal axes. In this way, the stack of acquired images can be directly transformed into a voxel-based data volume. The smallest voxel dimensions that can be reached at present are $6 \times 7 \times 17$ nm. In order to increase the number of sequential images, an automated procedure for slicing and imaging has been developed. As an example, FIB nanotomography is applied to the 3D analysis of a barium titanate (BaTiO_3) electroceramic body in a highly porous state as it exists after forming from a loose BaTiO_3 nanopowder by extrusion and before sintering to a dense body (Wegmann *et al.*, 2003). Comparison of structural data obtained from FIB nanotomography with physical measurements (MIP, laser granulometry of nanopowder) reveals the potential of this 3D analysis for the quantitative description of micro- and nanostructural features.

Three-dimensional microscopy

In general, tomography includes any method that reveals internal structural information within an object by mathematically reconstructing it from a series of projections. Conventionally, tomography can be performed using a variety of different signals (e.g. neutron beams, gamma rays, X-rays,

magnetic resonance, ultrasound) where absorption or scattering of the incident beam can be detected (Russ, 1999). One of the oldest and most widely used techniques in materials science and medical and biological applications is X-ray absorption tomography. With the development of synchrotron beam lines for X-ray tomography, the resolution has strongly improved in recent years. Nevertheless, voxel dimensions below 1 μm can hardly be attained at present and therefore, in many cases, the resolution of X-ray absorption tomography is insufficient for the investigation of nanostructured materials. For a more comprehensive review of synchrotron-based tomography methods, see for example Kaestner *et al.* (2003), Sutton *et al.* (2003) or Ito *et al.* (2003).

Higher resolution can be achieved if tomography is based on a rotational series of images from TXM or from TEM. Weiss *et al.* (2000) have presented an example of cryo-TXM in which 3D reconstructions of organelles in green alga reveal details down to 60 nm in size. Using high-angle annular-dark field STEM (HAADF STEM), Koguchi *et al.* (2001) successfully reconstructed the 3D topology of ZnO particles with fibre widths as small as 50 nm. A major drawback of both these transmission microscopy methods is the small sample size that is required for the material to become transparent to either electrons (TEM) or photons (TXM). For heterogeneous materials, the investigated sample volume in these thin sections may not be representative of the average internal structure. Thus, in order to obtain representative results from TEM or TXM tomography, either site-specific sampling or a large amount of data providing a statistical basis is required.

A different sector of 3D methods is provided by FIB procedures. This includes etching and sputtering techniques, combinations with secondary ion mass spectrometry (SIMS) and serial sectioning procedures. Layer-by-layer etching (Patkin & Morrison, 1982) and ion sputtering techniques (Hutter *et al.*, 1993) both rely on the assumption that material is uniformly removed from the sample. However, depth resolution degrades as material is removed (Ximen *et al.*, 1990) because of preferential sputtering at grain boundaries and also because of irregular redeposition of sputtered material on etched surfaces. The combination of FIB and SIMS enables the analysis of element distributions in three dimensions. For instance, Tomiyasu *et al.* (1998) have presented two different FIB-SIMS approaches: shave-off depth profiling and serial sectioning. With the shave-off method, a wedge of material is eroded and analysed simultaneously. Depth profiles can be calculated using mathematical deconvolution algorithms in the case where the geometry of the eroded body is well defined, e.g. when shaving off a segment from a spherical particle. A high depth resolution (± 5 nm) is achievable with the shave-off method, but a major drawback is the lack of a well-defined lateral resolution. This problem may be reduced by using the serial sectioning method, in which the ion beam is used for both in-plane FIB milling and angular SIMS excitation. Although SIMS analyses can achieve 50 nm of in-plane and

5 nm of depth resolution, the spacing between the individual FIB milling sections is in the micrometre range. Consequently, computational correlation procedures are necessary for a stereological 3D reconstruction. Thus, for both FIB–SIMS methods, shaving-off and serial sectioning, no voxel-based raw data can be obtained and the required stereological correlation procedures may introduce considerable errors.

Inkson *et al.* (2001a) presented a refinement of serial sectioning known as FIB tomography. In this method, the 3D reconstruction from electron images is devoted to microstructural but not to elemental analysis. In order to obtain an accurate overlay of a stack of images, a cross-correlation procedure with reference markers was introduced. In this way, boundaries of (sub)micrometre-sized grains in FeAl-based nanocomposites could be localized in 3D space with a precision better than 100 nm. A second application of FIB tomography presented by Inkson *et al.* (2001b) is the 3D mapping of Cu–Al multilayers after deformation by nano-indentation. It could be shown that the resulting deformation patterns (in three dimensions) are highly asymmetric and depend strongly on the tip geometry. Based on extracted deformation maps, the local variations of layer thicknesses ($x \times 10$ nm to $x \times 100$ nm) could be described quantitatively.

A major advantage of FIB tomography compared with other 3D methods is the fact that localized investigations on rather large samples can be performed (zoom-in function similar to SEM), which permits better control for representative analyses of heterogeneous structures. The resolution of single-beam FIB tomography, however, is limited by the relatively large and irregular spacing of 100–600 nm between the individual sections, which is mainly caused by the mechanical tilting and repositioning of the stage before and after each sectioning

and imaging step. Furthermore, a major source of error is the interpolation of structural features in the third dimension. Additionally, the sequential procedure with single-beam FIB is time consuming and the examples presented in the literature consist of no more than 10–20 images.

Refinement of the serial sectioning procedure for FIB nanotomography

Geometry and cube preparation

In order to refine the serial sectioning procedure, a dual-beam FIB (FEI Strata DB 235) was used in the current study. It consists of an ion optic column with a Ga^+ liquid metal ion source (LMIS) and an electron optic column (SEM) with a field emission gun (FEG). The sample is placed at the eucentric point where the two columns converge at an angle of 52° . Hence, while the ion beam can be used for precise sample manipulations (milling, cutting, polishing), the sectioned planes can be imaged with the electron column as in a conventional SEM. The principal geometry is shown in Fig. 1. During the serial sectioning process, the stage tilt is kept constant at 52° so that the sample surface (x – z plane) is perpendicular to the ion beam (y –direction). The FIB-prepared imaging planes are defined as x – y planes and their intersection with the sample surface as the x –direction. Secondary electron (SE) images of the x – y planes are taken from an angle of 52° . During the sectioning procedure, a series of layers are eroded with a constant thickness in the z –direction.

Before the actual serial sectioning procedure can be started, a cube of appropriate size has to be prepared (Fig. 1). Cube dimensions and corresponding sectioning and imaging para-

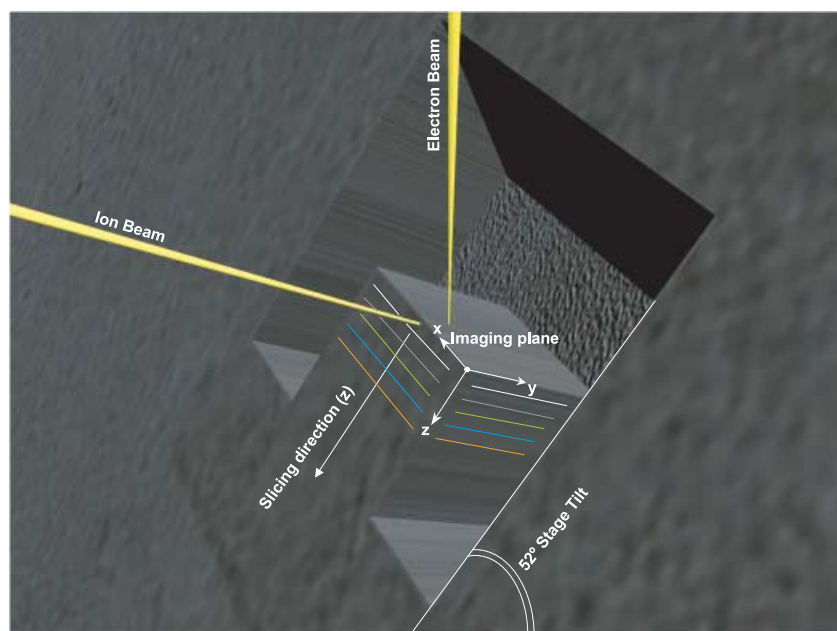
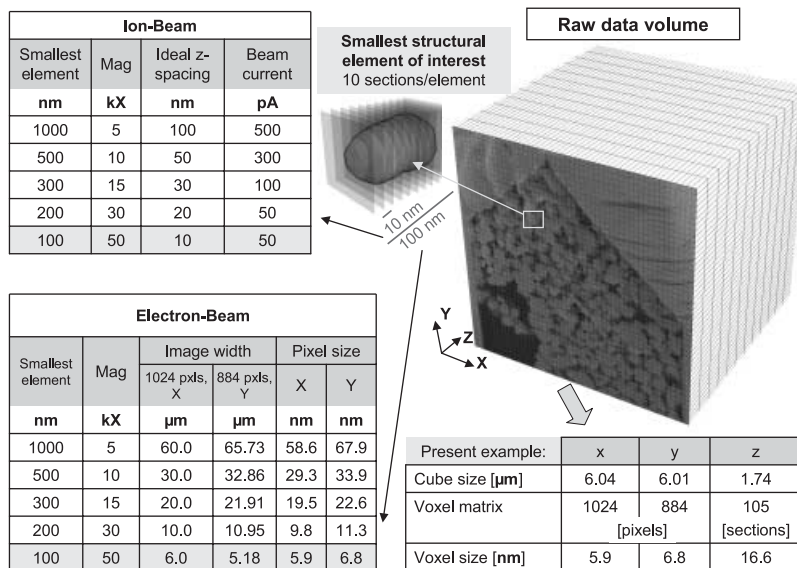


Fig. 1. Schematic illustration of a sample cube and geometrical relationships of the imaging plane with electron and ion beams.

Fig. 2. Empirical relationship between structural dimensions (i.e. fineness of microstructure) and the corresponding optimal settings for the ion and electron beams. The example highlighted in grey illustrates optimal settings for the 3D reconstruction of 100-nm-sized particles, which would require erosion of slices as thin as 10 nm. Voxel dimensions at the highest resolution that can be achieved at present are shown in the table at the bottom right. The voxel geometry in the raw data is distorted because the z-spacing (16.6 nm) is approximately three times larger than the corresponding pixel resolution (5.9×6.8 nm).



meters (e.g. ion-beam current, spot size, etc.) depend strongly on the required resolution. The relations between resolution and FIB/SEM parameters are discussed below (see Fig. 2). In order to render the x - y plane accessible for image acquisition with the electron beam, a trench has to be eroded in front of the cube. Additional trenches must also be eroded at both sides of the cube in order to avoid shadow-effects from the side walls. Such shadow-effects would induce uneven background grey levels, which cause problems during subsequent image processing (segmentation). Furthermore, overlay reference markers are needed to enable a precise overlay of the serial images. By using the FIB as an ion mill, precise markers can be produced by cutting the left and right upper edges of the cube under an angle of 45° each. The resulting planes will be visible on the sectioned planes as two reference lines that are perpendicular to each other. The last step of cube preparation is the deposition of a thick Pt or Au layer. The metal layer protects the overlay reference marks from undesired ion-induced erosion and, for non-conductive materials, the metal coating also reduces charging effects.

Serial sectioning procedure and related parameters

After preparing the cube, the serial sectioning procedure can be started. Serial sectioning is an alternating procedure in which first a thin layer of material from the cube face is precisely eroded with the ion beam and the newly exposed surface is subsequently imaged by SEM. For stacks with hundreds of sections, it is necessary to introduce an automated procedure for sectioning and imaging and, for this purpose, the AutoScript language for FEI workstations (FEI-Company, 2000) was used here. The automation procedure requires the definition of appropriate imaging and slicing parameters in advance. These parameters have to be optimized for both columns as a function

of the sample properties and dimensions of interest. Examples for empirically optimized parameters (ion and electron beam) related to the required magnifications and resolutions are shown in Fig. 2. The required resolution depends primarily on the dimensions of the smallest structural unit of interest (e.g. particle size or pore size). As a rule-of-thumb, at least ten sections are required per particle in order to obtain sufficient resolution for an accurate 3D reconstruction of the granular texture. The example in Fig. 2 highlighted in yellow represents ideal parameters (layer thickness of 10 nm) for the analysis of 100-nm-sized particles. At present, a resolution of 10 nm in the z -direction is difficult to attain. However, preliminary applications of FIB nanotomography confirm that 17 nm is achievable at present. For a reproducible erosion of these thin layers, a low ion beam current of approximately 50 pA has to be used. A magnification of 50 000 \times (or higher) is required for both electron and ion beams. For a stack of 105 images (i.e. the raw data for Figs 3–6 below), the data volume is then $6.01 \times 6.04 \times 1.74 \mu\text{m}$ with the corresponding voxel dimensions of $5.9 \times 6.8 \times 16.6$ nm.

Serial sectioning in general is a time-consuming process. However, by automating a number of operations, the acquisition time can be reduced considerably. The most time-consuming step is the SEM image acquisition itself. In the current case, relatively slow scan rates in the range of 60 s were chosen in order to obtain high signal-to-noise ratios. For the erosion of 17-nm-thick layers, only short ion milling times of less than 10 s are required. In addition, dead times of 10 s are necessary for re-equilibration after switching from one beam to the other. Ion-induced secondary electron (ISE) images, which are regularly taken for drift compensation (see below), lead to an additional retardation of 5–10 s. Thus, approximately 2 min are required for each layer and a stack of 100 images can be acquired within 3–4 h. Sample prepara-

tion, cube preparation and subsequent data processing are by far more time consuming than the sectioning procedure itself.

During the sectioning procedure, beam shift, sample drift and changes in the focal depth have to be corrected. The focus of the electron beam must be readjusted constantly because the imaging plane shifts to greater working distances as the cube is eroded away. This can be done either manually (by interrupting the procedure) or automatically (after a predefined interval of slices). Drift problems are more difficult to compensate for. Of particular importance is the displacement in the z -direction caused either by a shift of the ion beam or by a mechanical drift of the stage. Displacements in the z -direction potentially lead to irregular slicing step sizes and therefore, if not compensated, reduce 3D resolution and introduce an error. In order to measure drift in the z -direction, ISE images are taken from the sample surface (x - z plane) after each slicing step. The position of a reference marker is then compared with its initial position using pattern recognition algorithms. The ion beam is then automatically readjusted by varying the voltage of the beam-shift coils in order to correct for the measured drift. For this purpose, the ion-beam shift ($\mu\text{m V}^{-1}$) has to be calibrated prior to serial sectioning, which is an optional feature of the programmed AutoScript routine. As a result of the automated correction algorithms, possible drift phenomena in the x - z plane can be compensated for and the slicing thickness remains constant. Drift phenomena in the x - y plane are compensated by the digital overlay of serial images during computational analysis, using the reference markers mentioned above.

Charging is a major problem with non-conductive materials, which may diminish image quality considerably. In porous materials, charging may be reduced by impregnation with Wood's Metal (Bi-Pb-Sn-Cd alloy with a melting point of 70 °C). Alternatively, charging effects may be suppressed by using a negative detector bias. In this way, mainly back-scattered electrons are detected, which gives a good atomic-density contrast between different phases in a material, e.g. ceramic particles embedded in a polymer matrix.

Data processing and reconstruction of 3D structures

Image processing and 3D reconstruction includes the following steps: (a) correction of voxel dimensions for oblique-angle imaging (52°) and overlay correction for x - y drift (FIB-induced/electronic); (b) crop-out of a suitable subvolume; (c) segmentation/binarization; and (d) parametrization/measurements. Here, most steps of the data processing were performed using the Amira 3.1 software (see www.tgs.com). In addition, IDL 6.0 and Visual Basic were used for quantitative analysis.

(a) Correction of dimensions. The absolute dimensions in the x -direction are obtained from a calibrated FIB magnification scale. Because of oblique SEM imaging at an angle of 52°, distances in the y -direction have to be corrected for projection effects using $y' = y \times \sin(52^\circ)$. The z -values for each layer

are obtained from the measured cube thickness of the stack divided by the number of slices. This is equivalent to the thickness of each layer, which has been corrected for drift phenomena during the slicing procedure using ISE pattern recognition. Realignment of possible planar displacements between two subsequent slices can be achieved by iteratively transforming towards the location of the 2D correlation function maximum. Instead of using the entire image information, this process can be restricted to a predefined region of interest, which includes the reference markers.

(b) Crop-out of a subvolume. Given the entire body of data for the analysed cube, a subvolume has to be defined for further data processing. A representative subvolume should reflect the average microstructure of the sample. Reference markers and anomalous regions (e.g. low contrast, defective impregnation) should be excluded from this subvolume.

(c) Segmentation and visualization. After applying a median filter, binarization of the data volume is obtained by 3D thresholding. In order to obtain accurate results, good image quality (i.e. high contrast, low signal-to-noise ratio) is of particular importance. For this reason, long scan times must be used and charging effects minimized (as discussed above) during SEM image acquisition. For polygonal surface representation, wire frame structures, which are particularly suitable for 3D visualization, are calculated from the resulting binary voxel mask by applying the well-known 'marching cubes' algorithm (Lorensen & Cline, 1987) (see Fig. 6).

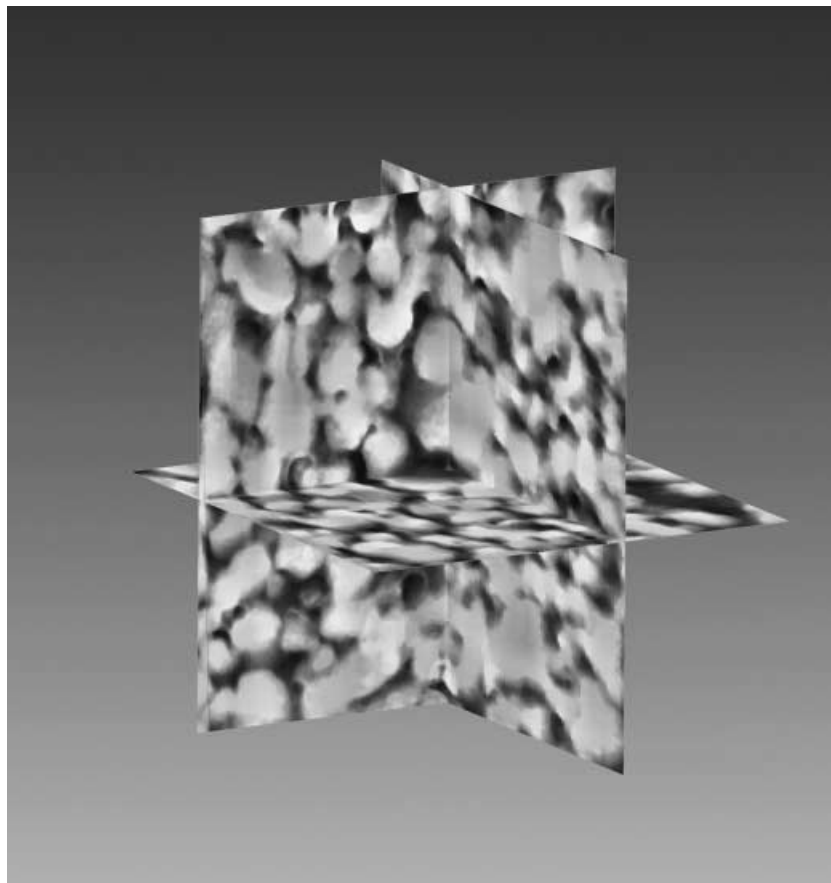
(d) Quantification/parametrization. The binary voxel data represent the basis for subsequent computational 3D analysis. Parameters such as volume fractions (from binary data) or surface area (from wire frame data) can be extracted easily. More advanced quantification such as the parametrization of networked structures requires detailed computational analysis. In the following section, examples of particle and pore size analyses based on 3D data from FIB nanotomography are presented and compared with physical measurements from the same material. It is beyond the scope of this paper to discuss geometrical analysis of microstructures in detail and we refer readers to the relevant literature (e.g. Delerue *et al.*, 1999; Ohser & Mücklich, 2000).

FIB nanotomography applied to BaTiO₃ ceramics

Material and sample preparation

In this study, FIB nanotomography was used to examine the microstructure of a porous ceramic body. The material was taken from an intermediate processing stage in the manufacture of BaTiO₃-based miniature positive temperature coefficient of resistivity (PTCR) elements by ceramic powder extrusion (Wegmann *et al.*, 2003). Particle size analysis of the starting nanopowder (La₂O₃-coated BaTiO₃ with sintering

Fig. 3. Orthogonal slices for 3D visualization of the microstructure in a BaTiO₃ sample. A series of 105 secondary electron images produced with FIB nanotomography is transformed into a voxel-based data volume. The orthogonal slices represent a matrix of $279 \times 269 \times 105$ voxels (voxel size: $5.9 \times 6.8 \times 16.6$ nm, total cube size $1646 \times 1829 \times 1743$ nm). For noise reduction a median filter is applied. (Orientation: x = (nearly) horizontal, y = vertical, z = depth.)



aid) showed that 10 vol.% of the particles are under 190 nm in size, 50 vol.% under 460 nm and 90 vol.% under 2000 nm (laser granulometry using a spherical particle approximation with a Malvern Mastersizer X after ultrasonication in deionized water). This powder was mixed with a paraffin-based thermoplastic binder in a 50 : 50 ratio by volume and the mixture subsequently extruded in the form of fine fibres. Prior to sintering of the material at temperatures in excess of 1200 °C to obtain the desired dense ceramic, the binder was removed by pyrolysis in air between 170 and 750 °C. It is in this highly porous so-called debound condition that the material was analysed here. The maximum temperature during thermal debinding was chosen to be below the temperature range at which solid-state sintering begins, i.e. where the powder particles begin to change shape and size due to diffusion. The retention of the original particle size and morphology was confirmed by SEM.

In preparation for FIB nanotomography, the pores in the sample were filled with epoxy resin by pressure impregnation. The sample dimensions were kept as small as possible (edge lengths of a few millimetres) in order to avoid mechanical stage drift during the slicing procedure. The sample was subsequently glued onto an aluminium stub and a location suitable for analysis identified by SEM, which was then stored for repositioning in FIB. Finally, a 25-nm-thick Pt layer was deposited by sputtering.

Reconstruction of 3D structures

Because the average particle size of the powder particles was in the range 200–500 nm, a sectioning step size of 17 nm was considered to be ideal for 3D reconstruction. A magnification factor of 50 000 \times was chosen for both beams. The ion beam was operated at 30 kV accelerating voltage and 50 pA beam current. A low accelerating voltage of 5 kV was used for SE imaging in order to minimize charging effects. Best contrast and resolution were obtained by spot size 2 and by setting the ‘through the lens-detector’ (TLD-D) into UHR mode. The scan times were 45 and 2 μ s per pixel for the electron and ion beams, respectively, resulting in image acquisition times of approximately 45 s by SEM and 2 s by ISE imaging. The acquisition time for a stack of 105 images was less than 4 h (without cube and reference marker preparation).

Following the steps described earlier for data processing, the stack was transformed into a voxel-based data volume. After correction for y -projection and z -drift, the voxel dimensions were $5.9 \times 6.8 \times 16.6$ nm. After overlay correction, a sub-volume with a voxel matrix of $279 \times 269 \times 105$ was cropped out. Figure 3 shows three orthogonal sections across this subvolume, which corresponds to a cube of $5.248 \mu\text{m}^3$ with dimensions of $1646 \times 1829 \times 1743$ nm. The grey values of

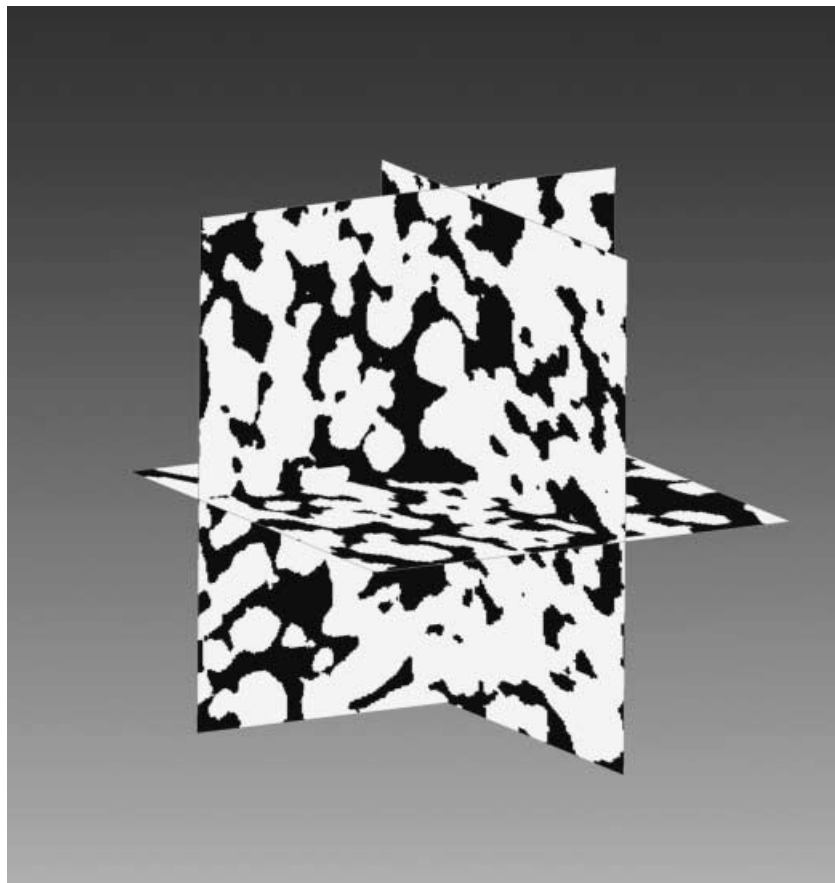


Fig. 4. Orthogonal slices of the same data volume as in Fig. 3 after binarization. The binarized data represent the basis for subsequent computational quantification and parametrization of the 3D structures. White areas represent BaTiO₃ particles, black areas pore space.

each voxel are based on the original grey values of the FIB/SEM images. A median filter was applied for noise reduction and a binary data volume was obtained by simple thresholding. In Fig. 4, the orthogonal slices shown in Fig. 3 are presented after binarization. The binary data represent the basis for most of the subsequent computational analyses, i.e. parametrization of the 3D structure.

Limitations in resolution and potential errors in thresholding become visible at a higher magnification. Figure 5 shows the magnified intersection of the three orthogonal planes. The horizontal x - z plane is shown in binary form, whereas the two other planes represent grey-scale data before thresholding. As can be seen in the grey-scale images, the boundaries between particles and pores are not defined as perfectly sharp lines, but rather as gradual transition zones with a width of a few voxels. The boundary between pores and particles may shift in this zone depending on the chosen threshold value. Segmentation by simple thresholding is thus one of the largest sources of uncertainty and potential error. More sophisticated methods such as edge-detection procedures and watershed segmentation may be applied in the future to minimize this problem. Even with such changes, however, the results will continue to be strongly dependent on the quality of the primary images: good contrast, low noise and high resolution

remain the critical parameters for accurate and reproducible results.

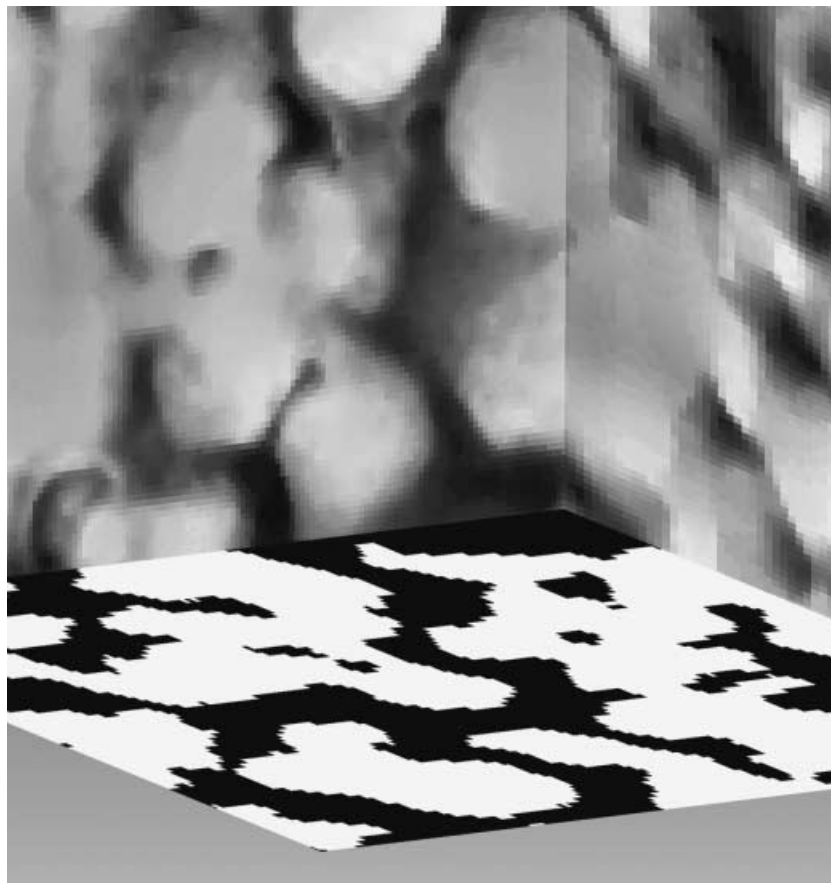
After segmentation, the pore volume was transformed into a polygon-based format (VRML). The triangulated surfaces of the porous and granular texture are shown in Fig. 6.

Quantitative analysis of 3D structures

Pore volume and particle volume were extracted from the binarized voxel data and surface area from the triangulated data. In the current example, the total pore volume (V) was determined to be $3.048 \mu\text{m}^3$. Because the total size of the analysed subvolume is $5.248 \mu\text{m}^3$, this results in a volume fraction of 41.9% for particles and 58.1% for porosity. This does not correlate well with the bulk 50 : 50 ceramic-binder volume ratio of the extrusion mixture; however, it does reflect the localized occurrence of large flattened pores (see Fig. 7) attributed to the pooling and shearing of excess binder in the mixture (Wegmann *et al.*, unpublished data). The lower right-hand corner of the cube in Fig. 6 is missing, indicating the inclusion of such a large pore in the sampling volume and explaining the pore-volume bias in the porosity calculation.

A surface area (S) of $64.821 \mu\text{m}^2$ is obtained for the interface between particles and porosity. From these data, an average

Fig. 5. Magnification of the intersection region of orthogonal planes shown in Figs 3 and 4. The horizontal plane (x - z plane) is binarized. Uncertainties associated with thresholding are discussed in the text. From the y - z plane on the right side it can be observed that the resolution in the slicing direction (z -direction, 16.6 nm) is slightly lower than in the original imaging plane (compare x - y plane, upper left, 5.9×6.8 nm).



particle diameter (D) can be calculated using the formula $6 \cdot V/S = D$. This formula is frequently used in the context of surface area analysis with the BET-method (Brunauer *et al.*, 1938). In the sample under consideration, an average particle diameter of 203 nm is calculated based on data from FIB nanotomography. This average particle diameter extracted from the 3D data is of the same order as, but larger than, the 151 nm calculated from a BET surface area measurement for the bulk raw powder (specific surface area = $6.6 \text{ m}^2 \text{ g}^{-1}$) and again reflects the effect of the cube intersection with the large pore and the associated missing particle surface area. Both surface-area-derived diameters are clearly smaller than the d_{50} of 460 nm determined by laser granulometry. From visual inspection of Fig. 6, it can be seen that the diameter of the BaTiO_3 particles rarely exceeds 350 nm. Thus, the average particle diameter of 460 nm obtained by granulometry is concluded to be an overestimation caused by the agglomeration of particles in the raw powder and/or errors introduced into the measurement by assumptions regarding particle sphericity and the refractive index of the material.

Further quantitative parametrization of the microstructure requires more detailed analysis and data processing. In the present study, pore-size analysis was performed following a similar procedure as described in Delerue *et al.* (1999). In a

first step, the pore network is skeletonized. The pore space is then virtually filled with spheres whose centres are located on the skeleton. The radii of the spheres reflect the shortest distance from the skeleton to the pore surface. The pore-size distribution is then obtained by summation of sphere volumes and classification according to the corresponding sphere radii.

In Fig. 8, the pore size distribution derived from 3D analysis is compared with the one obtained using MIP (CE Instruments Ltd, Model 140/440). The curves differ significantly at diameters greater than 100 nm. The curve obtained from 3D analysis shows a uniform distribution with a linear shape between 50 and 800 nm, which is in strong contrast to the MIP curve that exhibits a significant discontinuity at approximately 100 nm. In the MIP data, 80 vol.% of the pores apparently have radii below 200 nm and 50 vol.% of these have radii between 50 and 100 nm.

The difference between the two curves reveals the so-called ink-bottle effect affecting MIP. The radii (r) in MIP are calculated by an inverse proportional relationship from the corresponding pressures (p), i.e. from the Washburn equation $r = -F \cdot \gamma \cdot \cos \theta / p$ where F = form factor, γ = surface tension, θ = contact angle and p = pressure (Washburn, 1921). During the intrusion process, large pressures have to be applied in

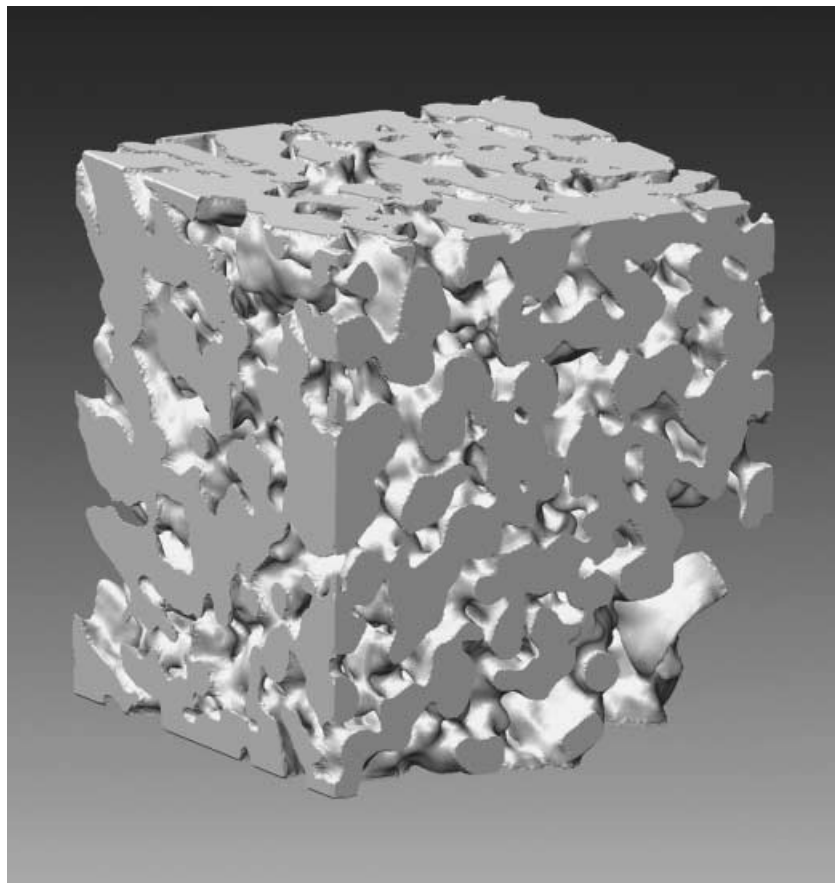


Fig. 6. Surface visualization of granular texture in the BaTiO_3 sample, which represents the same subvolume as in Figs 3 and 4. Cube dimensions: $1646 \times 1829 \times 1743$ nm.

order to fill larger pores over narrow pore necks. In this situation, the Washburn equation is not longer valid because the volume of larger pores is erroneously linked to the small radius of pore necks. The apparent accumulation of pores with radii of 50–100 nm in the MIP curve cannot be confirmed by visual investigation of the pore structure (Fig. 6) and these are therefore interpreted as an artificial phenomena related to the ink-bottle effect. Reconstructed 3D structures and related pore size distribution curves indicate that the measured 50–100 nm more likely reflect the typical dimensions of the pore necks within the porous network.

Estimation of uncertainties

In principle, two groups of error sources can be distinguished. First, the raw data include imperfections related to the image acquisition with FIB nanotomography (error classes I to III below) and, secondly, the subsequent computational analysis of the acquired data will introduce additional uncertainties (error class IV):

(I) As a primary source of error, one has to consider the accuracy of the magnification scale on the SEM images (x – y planes). This error source is directly related to the accuracy of the electron-beam calibration. In our FIB laboratory, the

calibration procedure guarantees a maximum error on the magnification scale below 3%. Thus, for images with pixel dimensions of 6 nm (as presented in our example), the systematic error is smaller than 0.18 nm per pixel (in the x - and y -directions).

(II) The roughness of the FIB-milled x – y plane introduces a certain error component on the z -axis. The roughness is influenced by the precision of the ion beam and of related milling capabilities, which themselves are strongly dependent on microscope settings such as magnification, spot size, beam current, milling time and the fine-tuning of the ion beam (focus and correction of astigmatism). Furthermore, the roughness is also strongly influenced by characteristics of the sample such as homogeneity and resistance of the material against milling. In order to quantify the roughness on FIB-milled planes, AFM investigations were undertaken on samples which were produced with milling parameters comparable with those used in our example with BaTiO_3 . The AFM results show that the elevations (in the z -direction) between ripples and valleys are generally below 1 nm.

(III) A further error component affecting the z -axis is related to drift phenomena and to the precision of the automated drift correction procedure. A drift rate of 2 nm min^{-1}

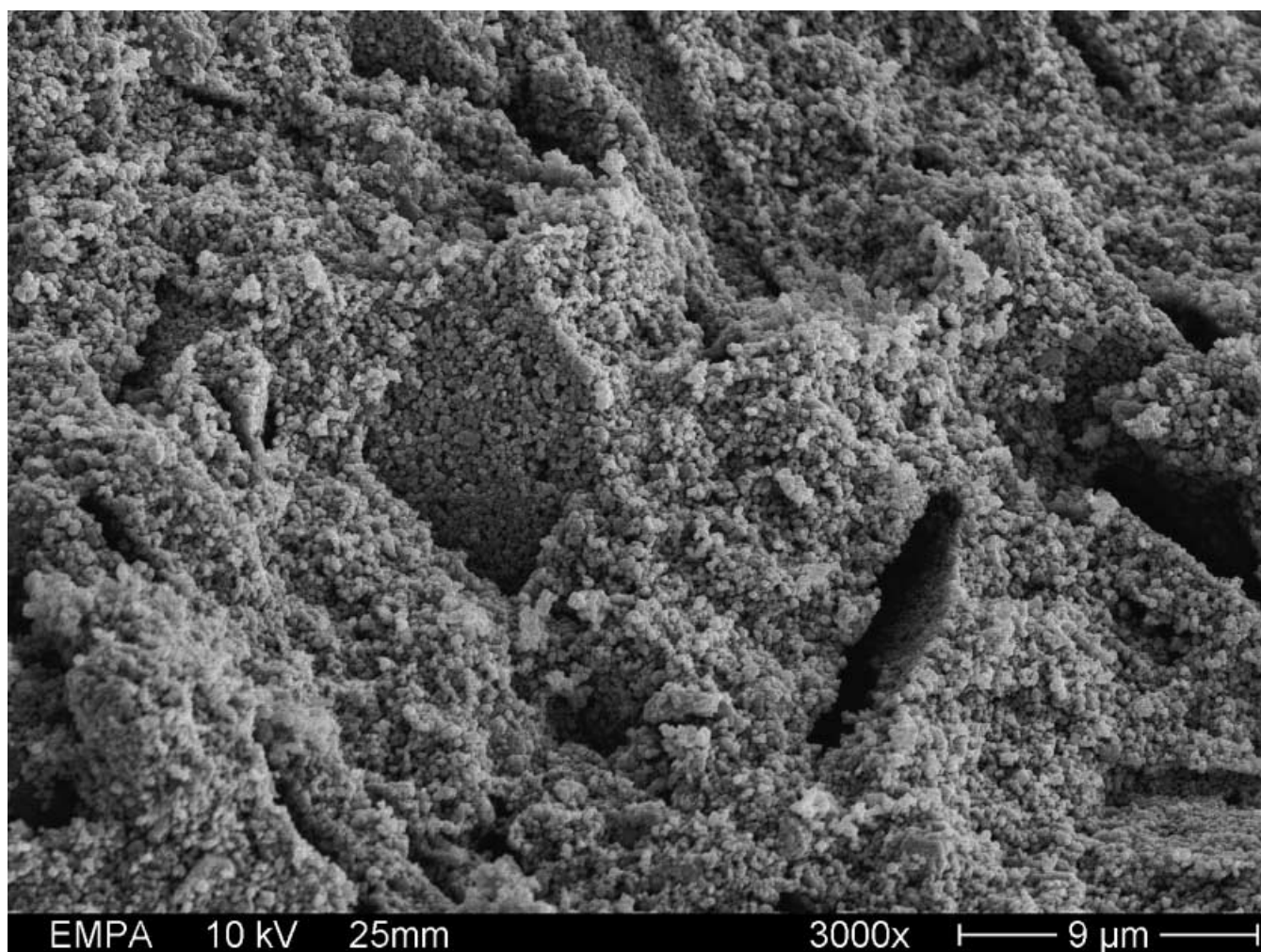


Fig. 7. SEM image of a fracture surface of the thermally debound extrusion composition used in this study, showing the large flattened pores assumed to stem from molten excess binder pooling to minimize free energy.

(which is typically observed, although usually with some fluctuations) will hardly affect the result when the slicing distance is 100 nm or more. However, in our example, in which a slice of only 17 nm is milled every 2 min, this drift rate will introduce an error of 24% on the z -axis. Thus, the higher the magnification, the higher also is the influence of drift, and the more important drift correction becomes. The precision of drift correction depends on many factors such as the quality of the ion imaging (contrast, focus, noise), the quality of the reference pattern (imaging with the ion beam may cause alterations with increasing number of slices), the accuracy of the pattern recognition procedure for measurement of drift (this is a Cognex command, which includes a user-defined variable for matching tolerance) and the accuracy of the beam shift for compensation of the measured drift (which is dependent on beam shift calibration – $V \mu m^{-1}$). Here, the most important error component is related to uncertainties in the drift measurement, which is limited by the pixel resolution of

the ion images. In our example, the precision of drift measurement by pattern recognition is assumed to be within the range of 2 pixels (i.e. < 12 nm). Because drift correction performs a relocalization for each of the slices relative to an absolute reference mark, this error remains the same for the entire stack of images, independent of the number of images within the stack. Consequently, the error for the average slicing thickness is smoothed out over the entire stack (in our example: < 12 nm divided by 105 slices).

(IV) Three different error sources in the computational processing of data have to be considered: (a) noise reduction by the median filter, (b) alignment of the image stack by overlay-correction for x – y shifts and (c) segmentation/binarization by thresholding.

(a) Smooth median filters only induce very localized changes of the image information. Because the locus of edges is preserved (in contrast to Gaussian filters), the errors from median filtering with a 5×5 kernel are negligible.

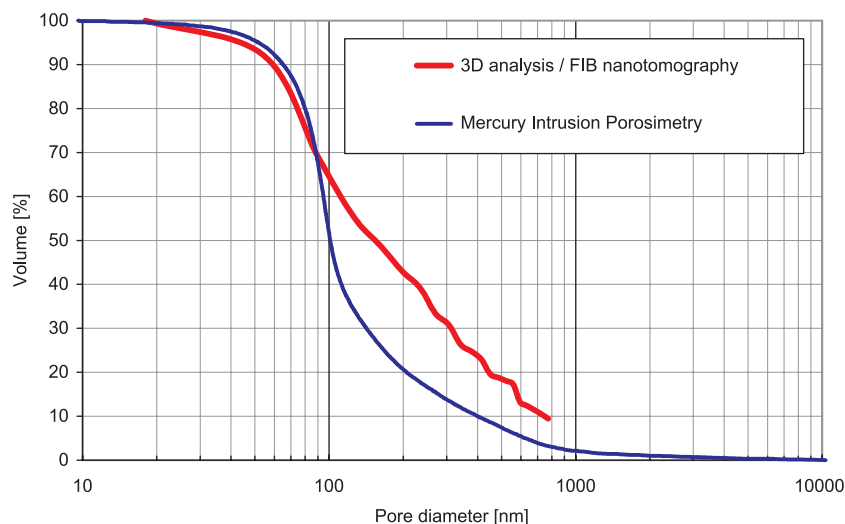


Fig. 8. Pore size distributions of the BaTiO₃ sample obtained by mercury intrusion porosimetry and by 3D analysis with FIB nanotomography. Details are discussed in the text.

(b) The precision of the overlay correction is observed to be very good (less than 2 pixels in the x - and y -directions). Furthermore, this error is random and will therefore be smoothed out over the entire stack.

(c) By far the most important error from data processing is introduced during segmentation. Here, the uncertainty of the binarization process by thresholding is strongly dependent on the image quality (mainly contrast). As shown in Fig. 6, the particle boundaries do not reveal sharp lines, being defined instead by a greyscale gradient that extends over a distance of approximately 3–5 pixels. In our example, this zone is thus 18–30 nm wide. In the ideal case, a threshold value is chosen so that the particle boundary in the binarized data reflects the centre of this zone. The maximum error is thus considered to be half the width of this zone (i.e. 9–15 nm in our example).

In summary, all potential error sources for FIB nanotomography are clearly dominated by uncertainties in the thresholding process for binarization. The accuracy of thresholding depends on the image quality, which itself includes many different parameters and effects (density contrast of materials within the sample, beam–sample interactions, signal emission, signal detection, microscope settings). However, a theoretical treatment of these parameters is beyond the scope of this discussion.

Because quantification of errors is very difficult and the relative importance of potential errors increases with the fineness of the microstructure, we are currently performing a calibration of the FIB nanotomography method at various magnifications. For this purpose we are using monosized nanoparticles as reference material with different particle diameters for different reference samples. In this way, the results from FIB nanotomography can be compared with calculated values of the reference samples (pore volume, surface area, particle diameter) and the overall methodical error can be quantified as a function of magnification and particle diameter, which correlates with the fineness of the microstructure.

Conclusions

Dual-beam FIB enables the acquisition of serial images with small and reproducible spacings between the single imaging planes because no mechanical stage tilting is necessary between the FIB milling and SEM imaging steps. By refining the automated serial sectioning procedure, a minimal step size of 17 nm can be reached at present with FIB nanotomography. Distances between the single imaging planes are thus nearly in the same range as the pixel dimensions within the imaging plane. For subsequent 3D reconstruction, the stack of images can easily be transformed into a voxel-based matrix due to the nearly equidimensional structure of the data volume. This is in strong contrast to conventional serial sectioning methods, in which a relatively large step size between the single imaging planes requires stereological correlation procedures for 3D reconstruction, which introduce considerable errors. Consequently, the acquisition of voxel-based data volumes with FIB nanotomography opens a new field of 3D scanning microscopy at high resolution with high accuracy.

In comparison with other tomography methods, FIB nanotomography fills a technological gap with respect to resolution and the sample volume under investigation: with voxel dimensions in the range of 10 nm, FIB nanotomography has the potential to resolve nanostructures that cannot be detected with absorption or scattering tomography methods which analyse coarser structures from larger sample volumes. On the other hand, high-resolution tomography based on X-ray or electron transmission may reach similar, or even better, resolution than FIB, but only for very thin samples. The investigated volume in FIB nanotomography is generally larger than in transmission microscopy and depends on various factors such as magnification, sectioning step size and number of acquired sections.

In this study, FIB nanotomography was applied to a porous ceramic consisting of BaTiO₃ nanoparticles. Significant

differences were observed when microstructural parameters extracted from 3D reconstructions are compared with physical measurements. The pore size distribution obtained from mercury intrusion porosimetry appears to be strongly affected by the geometry of pore necks, which lead to an overestimation of the fine structured pore volume with radii of 50–100 nm. Pore size analysis based on FIB 3D reconstruction shows a more realistic pore size distribution with a linear curve between 50 and 800 nm. Similarly, it can be shown that physical particle size analyses with laser granulometry may be affected by particle agglomeration in the raw powder and calculation assumptions that lead to an overestimation of the concentration of large particles.

These investigations on nanoporous BaTiO₃ document the ability of FIB nanotomography to reconstruct 3D structures with dimensions in the range of 100 nm or even smaller. Such 3D reconstructions can serve as a basis for quantitative mathematical analysis of complex granular textures and of porous networks. Furthermore, they may also serve as a basis for computational modelling and simulation, e.g. of transport processes within the porous networks, or of degradation and failure processes in finely structured materials. Hence, FIB nanotomography may contribute important 3D data that may potentially help to improve our understanding of the link between microstructures with the corresponding material properties on a macroscopic scale.

Acknowledgements

We wish to thank Dr J. Kaufmann for fruitful discussions and for assistance with sample preparation. The suggestions of an anonymous referee are gratefully acknowledged. This work was financially supported by the EMPA fund for student exchange. The dual-beam FIB facilities are provided by the laboratory for electronics and metrology at EMPA.

References

- Brunauer, S., Emmet, P.H. & Teller, E. (1938) Adsorption of gas in multi-molecular layers. *J. Am. Chem. Soc.* **60**, 309–319.
- Delerue, J.F., Perrier, E., Yu, Z.Y. & Velde, B. (1999) New algorithms in 3D image analysis and their application to the measurement of a spatialized pore size distribution in soils. *Physics Chem. Earth – Part A*, **24**, 639–644.
- Diamond, S. (2000) Mercury porosimetry – An inappropriate method for the measurement of pore size distributions in cement-based materials. *Cement Concrete Res.* **30**, 1517–1525.
- FEI Company (2000) *AutoScript*, Technical Note PN 25564-C. FEI Company.
- Hutter, H., Wilhartitz, P. & Grasserbauer, M. (1993) Topochemical characterization of materials using 3D-SIMS. *Fresenius J. Anal. Chem.* **346**, 66–68.
- Inkson, B.J., Mulvihill, M. & Möbus, G. (2001a) 3D determination of grain shape in a FeAl-based nanocomposite by 3D FIB tomography. *Scripta Mater.* **45**, 753–758.
- Inkson, B.J., Steer, T., Möbus, G. & Wagner, T. (2001b) Subsurface nanoindentation deformation of Cu-Al multilayers mapped in 3D by focused ion beam microscopy. *J. Microsc.* **201**, 256–269.
- Ito, M., Ejiri, S., Jinnai, H., Kono, J., Ikeda, S., Nishida, A., Uesugi, K., Yagi, N., Tanaka, M. & Hayashi, K. (2003) Bone structure and mineralization demonstrated using synchrotron radiation computed tomography (SR-CT) in animal models: preliminary findings. *J. Bone Mineral Metab.* **21**, 287–293.
- Kaestner, A., Lehmann, P., Wyss, P. & Flühler, H. (2003) Synchrotron tomography to map the pore structure of sandsamples. *Geophys. Res. Abstracts*, **5**, 11095.
- Koguchi, M., Kakibayashi, H., Tsuneta, R., Yamaoka, M., Niino, T., Tanaka, N., Kase, K. & Iwaki, M. (2001) Three-dimensional STEM for observing nanostructures. *J. Electron Microsc.* **50**, 235–241.
- Lorensen, W.E. & Cline, H.E. (1987) Marching cubes: a high resolution 3D surface construction algorithm. *Computer Graphics*, **21**, 163–169.
- Meyer, E., Hug, H.J. & Bennewitz, R. (2004) *Scanning Probe Microscopy. The Lab on a Tip*. Springer, London.
- Ohser, J. & Mücklich, F. (2000) *Statistical Analysis of Microstructures in Materials Science*. Wiley, Chichester.
- Patkin, A.J. & Morrison, G.H. (1982) Secondary ion mass spectrometric image depth profiling for three-dimensional elemental analysis. *Anal. Chem.* **54**, 2–5.
- Russ, J.C. (1999) 3D image acquisition. *The Image Processing Handbook*, pp. 575–616. CRC Press, Boca Raton, FL.
- Sutton, S.R., Newville, M. & Rivers, M.L. (2003) Synchrotron X-ray microprobe analysis. *Geophys. Res. Abstracts*, **5**, 13260.
- Tomiyasu, B., Fukuju, I., Komatsubara, H., Owari, M. & Nihei, Y. (1998) High spatial resolution 3D analysis of materials using gallium focused ion beam secondary ion mass spectrometry (FIB SIMS). *Nuclear Instruments Meth. Phys. Res. B* **136–138**, 1028–1033.
- Washburn, E.W. (1921) Note on a method of determining the distribution of pore sizes in a porous material. *Proc. Natl Acad. Sci. USA*, **7**, 115–116.
- Wegmann, M., Clemens, F., Graule, T. & Hendry, A. (2003) Microextrusion of lanthanide-doped barium titanate for PTCR applications. *Am. Ceramic Soc. Bull.* **8**, 9501–9508.
- Weiss, D., Schneider, G., Niemann, B., Guttman, P., Rudolph, D. & Schmahl, G. (2000) Computed tomography of cryogenic biological specimens based on X-ray microscopic images. *Ultramicroscopy*, **84**, 185–197.
- Williams, D.B. & Carter, C.B. (1996) *Transmission Electron Microscopy – a Textbook for Materials Science*. Plenum Press, New York.
- Ximen, H., DeFreez, R.K., Orloff, J., Elliott, R.A., Evans, G.A., Carlson, N.W., Lurie, M. & Bour, D.P. (1990) Focused ion beam micromachined three-dimensional features by means of a digital scan. *J. Vac. Sci. Technol. B*, **8**, 1361–1365.